Fatigue crack growth rate at material and geometry transitions in glass-epoxy composites

S. Goutianos [a,*], B.F. Sørensen [b]

[a] Department of Manufacturing and Civil Engineering, Norwegian University of Science and Technology, Teknologivegen 22, 2815 Gjøvik, Norway
[b] Department of Wind Energy, Section of Composite Mechanics and Structures, Technical University of Denmark, Risø Campus, DK-4000 Roskilde, Denmark

ARTICLE INFO

ABSTRACT

An element test specimen with ply drops, intended to be representative of a composite structure of varying thickness such as the main laminate in a wind turbine rotor blade structure, is used to investigate the fatigue damage initiating from a ply drop under cyclic tension–tension loading. The focus is to measure the growth rate of delamination cracks propagating from a thin towards a thicker section. Several delaminations initiate from tunneling cracks - cracks between the ply drops and resin reach areas - after very few load cycles. All except one delamination crack propagate for a number of cycles but eventually stop growing. The only delamination crack that continued to grow has the characteristic that its growth rate increases as it propagates to thicker sections of the element specimen. The experimental findings are supported by finite element results.

1. Introduction

The external shape of many large lightweight composite structures such as wind turbine rotor blades is dictated by aerodynamic considerations. The need to reduce weight leads to designs with composite laminates of varying thickness along the length of the structure or component, with the requirement of retaining sufficient stiffness, strength and fatigue life [1]. In composite structures, a decrease in laminate thickness (tapering), for shape optimisation and weight reduction, is achieved by terminating or dropping off plies (ply drops) at the locations where a change in thickness is required [2]. A ply drop results in material and geometrical discontinuities which induce stress concentrations and can be a site for crack initiation and propagation in service [3,4] and thus reduces the load carrying capability of a composite structure.

Most studies on ply drops are related to aerospace applications such as aircraft wings or fins and helicopter blades [2,5,6]. Even for thin laminates, as used in aerospace structures (prepreg based composites), ply drops are critical locations for delamination initiation that can lead to premature failure of components [4]. In applications involving large structures/components made by low-cost manufacturing processes, e.g. wind turbine blades produced by vacuum infusion, the plies are thicker (about 1 mm in thickness) [4] and thus ply drops have a stronger influence on the structural integrity of the component. The studies investigated the effect of ply drops in such composite structures

[4,7,8] have shown a relative high knockdown factor, i.e. a significant reduced strength and fatigue life, with increasing ply thickness.

Tapering of laminates by ply-drops can be achieved in several different ways [9,10], from dropping off several plies in one step (all at one location) to dropping plies in a staircase-like arrangement to have a gradual transition. From a manufacturing point of view, the first approach is advantageous since it is does not increase the manufacturing cost [11]. However, it leads to designs that are more susceptible to delaminations [8]. Therefore, most efforts are towards taper designs using staircase-like arrangements where the ply drops are relative close, but with a certain distance between successive ply drops [9]. Interleaving the dropped plies between continuous plies is also an effective approach to increase the delamination resistance [11]. The disadvantage of these approaches is that they increase manufacturing cost as it involves detailed planning of the lay-up [8]. Different ply drops staggered configurations have been investigated experimentally and analysed numerically [12–15]. In the staggered ply drop designs, a small amount of resin (resin pocket) is trapped between the ply drop and the surrounding continuous plies [9,16]. Crack initiation and delamination between the dropped and continuous ply has been experimentally observed and predicted by numerical models [1,6,9,10,17,15]. The formation of such a delamination probably cannot be suppressed by any conventional ply drop design. To overcome this issue, Khan et al. [11] proposed a new design, a chamfered ply drop geometry to minimise the size of the resin pocket. Ply edge cham-

fering nearly eliminated resin accumulation at the ply drop, and the resulting static strength and fatigue lifetime were significantly increased in comparison with a design using a traditional non-chamfered ply drop [11].

From the above, it is clear that delamination can start from ply drops. Even for chamfered ply drops, delaminations will most likely initiate under cyclic loading although the cycles for crack initiation may be significantly higher than for laminates with conventional ply drop geometries. In the manufacture of a large structure there is a high probability that some of the plies are not perfectly placed in the mould and thus even for chamfered ply drops, resin rich areas can be expected in some ply drop locations. Thus, defects and damage at such critical sites should be addressed in the design of such structures. A conservative approach with large safety factors, aims to prevent crack initiation, leads to structures which are far from optimum. An alternative approach is to design in accordance with the concept of damage tolerance, which was first introduced in the fv aerospace sector in the 1970ies to obtain cost-effective light-weight structures [18–21]. With this approach, a structure can sustain a certain damage that propagates slowly (stably) and will be detected by non-destructive techniques (NDT) in regular inspection intervals and will then be repaired [22]. A more advanced concept is based on structural health monitoring to detect damage in service by built-in sensors and an NDT inspection will only be conducted when damage is detected [23]. Understanding the sequence of damage initiation from a ply drop and the damage evolution is thus important in designing a composite structure of complex shape and forms the basis for defining an inspection/monitoring plan. This approach potentially leads to larger weight savings.

1.1. Problem statement

In the present work, an element test specimen containing four ply drops (Fig. 1) is designed with the purpose to examine damage initiation and propagation from ply drops experimentally under cyclic tensile loading. The investigation covers damage initiation at a ply drop but the focus is on the subsequent crack/delamination growth rate dependence on ply drop geometry. For this reason, conventional ply drops with resin pockets, are used. Fig. 1 shows a schematic drawing of part of the element specimen containing two ply drops with some distance between them. At each ply drop, a resin pocket will form during manufacturing. By using a certain spacing (in x_1 direction) between the two ply drops, it is possible to study the ply drop interaction and measure the cyclic delamination crack growth rates of the two delaminations independently. In the present study, the composite material used is a typical material for wind turbine blades with relatively thick ply drops with a ply/layer thickness in the order of a millimeter.

An element test specimen (Fig. 1) containing design details i.e. as ply drops is indented to replicate the damage modes of real structures. An element test is a test specimen between coupon test and substructure test. Typical laminates for a load carrying component of a wind turbine blade consist mainly of unidirectional plies with $\pm 45°$ (biax) fabrics on the outer layers. Therefore such a layup is used in the present study. The presence of the support/backing threads results in weak interfaces between the layers of the specimen where a delamination can initiate and propagate [24]. It should be mentioned that an element test is different from a sub-component test, where the sub-component is usually a real design detail or a cut-out from the structure [25]. An element test specimen is a purposely designed test specimen that will develop several competing failure and damage types, designed to study the evolution and interaction of the basic failure modes. An element test specimen is thus expected to develop similar damage as real structures, but is indented to give a more clear insight in the damage evolution than real structures.

In order to help the interpretations of the experiments, finite element analyses are used. The ply drop interaction is investigated using a cohesive zone based finite element analysis, whereas crack growth in the specimen's constant thickness region is analysed by a linear elastic fracture mechanics based finite element model. The present element specimen was designed to be relative long to enable delamination cracks to extend a relative long distance away between the grips (to investigate if crack growth rate became constant), and to minimize bending, so that the specimen can analyzed by a simple analytical model (A). The spacing between the first and second ply-drop were chosen to be relative short in order to study the interaction of the cracks emerging from the two ply-drops.

2. Experimental procedure

2.1. Materials

A unidirectional (0°) glass fibre fabric with support/backing threads in 90° was obtained from Saertex GmbH, Saerbeck, Germany. The fibre diameter in the 0° glass rovings, with 2400 *tex*, was 17 μm, and the area weight was 1134 g/m². The glass fibres in the support
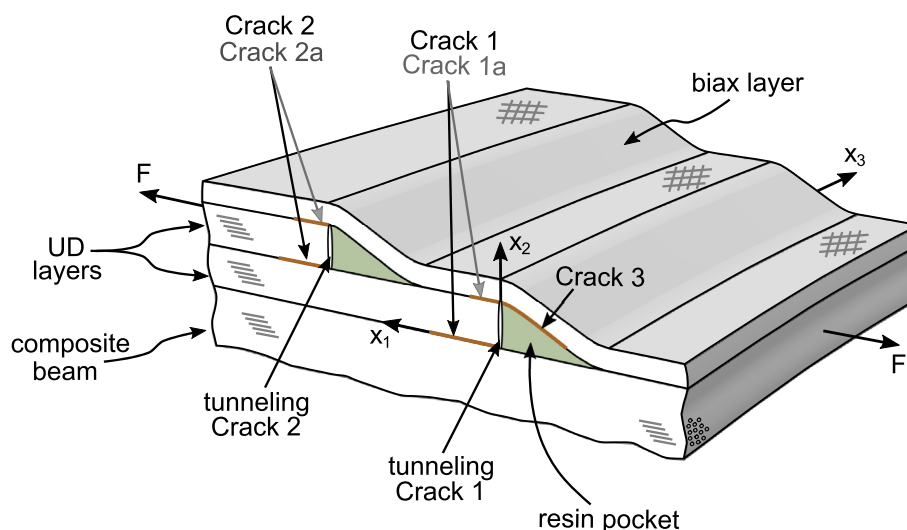

Fig. 1. Schematic drawing of two ply drops close to each other. The possible cracks, tunneling cracks and delamination cracks, are shown.

threads (68 *tex*) had a diameter of 10 μm and an area weight of 54 g/m^2. Polyester fibres with 110 *tex* and area weight of 12 g/m^2 were used as sewing threads in a tricot-warp stitching pattern.

A biaxial glass fibre fabric ($\pm$45°) with a total area weight of 720 g/m^2 was obtained from Ahlstrom, Tampere, Finland. The area weight of the $\pm$45° fibres (600 *tex*) was 592 g/m^2. The support threads, glass fibres with 200 *tex*, had an area weight of 19 g/m^2. The biaxial fabric included a chopped strand mat layer with 100 g/m^2 and 30 *tex*. The glass fibre diameter was 16 μm, except the chopped strand mat which made of glass fibres with a diameter of 12 μm. The stitching yarns were constructed from polyester yarns with 76 *tex*. The fabric structure has a strong influence on the interface/ cohesive law properties between the layers.

Epoxy was used as a matrix material. The epoxy resin, Araldite® LY 1568, and the hardener, Aradur® 3489 CH, were provided by Huntsman Advanced Materials GmbH, Basel, Switzerland.

2.2. Manufacturing of element specimen with ply drops

Ten unidirectional plies/layers, all 700 mm in length, were placed on the surface of a vacuum infusion table to form a composite plate consisting of UD layers. Four unidirectional plies, each having different length, were placed on top of the ten unidirectional plies to create four ply drops (see Fig. 2). Finally, a continuous biax fabric layer was placed on top of the four unidirectional plies and the composite beam as shown in Fig. 2.

All layers (0° and $\pm$45°) were placed with the support/backing threads (90°) facing downwards (the direction opposite to the x_2 axis shown in Fig. 2) and and as can be seen in the scanning electron microscopy images in Fig. 3.

After laying all fabric layers, a vacuum bag was applied and the epoxy resin was infused. Then, to cure the resin, the plate (700 × 400 mm^2) was heated at 40°C for 19 h, followed by a heat-up to 75°C for 5 h and cooled down. After curing, the thickness of each unidirectional layer was approximately 0.9 mm and the thickness of the biax layer was about 0.6 mm. The fibre volume fraction in the unidirectional layers was 50%. During infusion, resin pockets had formed at each ply drop as schematically shown in Fig. 2. The precise shape of the resin pockets was to some extend controlled by the vacuum infusion process. The resin pocket length, in x_1 direction, was between 3.0 and 3.2 mm and the angle between 14 and 16°.

Glass fibre epoxy composite tabs (1.8 mm thick) were glued on the thin section of the plate (see Fig. 2) so that this end would have the same thickness as the other end. As a result, the specimen would be aligned with the loading axis when mounted at the testing machine. The ply drop specimens were cut-out from the plate in a width of 30 mm. Their dimensions along the length are given in Fig. 2. The distance between ply drops 1 and 2, which are being used in the present paper, was approximately $d = 10$ mm.

Prior to testing, details of the ply drop were investigated by scanning electron microscope (Zeiss Evo 60 EP-SEM) using a secondary electron detector. An example is given in Fig. 3.

The modulus of the UD plies, in the fibre direction, was measured by statically testing ply drop specimens similar to Fig. 2 but without the biaxial layer. The strain in the thin section of the ply drop specimens were measured by two strain gauges on opposite faces of the specimen. The Young's modulus was equal approximately equal to 38 GPa.

It should be emphasized that the current element test specimen is not an exact representation of a wind turbine substructure. The present work focuses on how such an element test can be designed and analysed.

2.3. Test procedure

The specimens were subjected to cyclic loading on an Instron 8800 servo–hydraulic testing machine with a 250 kN load cell under load control at an *R*-ratio ($R = \sigma_{min}/\sigma_{max}$) of 0.1. The minimum and maximum stress values σ_{min} and σ_{max} were calculated by dividing the values of the minimum and maximum loads with the cross-sectional area of the thin section of the ply drop specimens (between ply drop 1 and tab, Fig. 2). The loading frequency was set to 3 Hz (a higher loading frequency could induce heating of the specimen during cyclic loading). The position of the cross-head and maximum and minimum loads for each cycle were recorded.

The delaminations/cracks length was monitored from images recorded by a digital camera. Digital images (2592 × 3872 pixels) were acquired automatically at a rate of 1 image per cycle for the first 100 cycles, 1 image for every 10th cycles in the range 100 to 1000 cycles, 1 image for every 100th cycles in the range 1000 to 10000 cycles etc. The image resolution was ≈0.04 mm/pixel. The camera was synchronised with the testing machine to acquire the images at the instant the specimen was subjected to the maximum load during a loading cycle. The delamination/crack length was easier to measure in the $x_1 - x_3$ plane (see Fig. 4) than in the $x_1 - x_2$ plane. The delamination/crack lengths were measured from the images using the ImageJ software [26]. As can be seen in Fig. 4, the ply drop specimen was partially transparent and this allowed accurate measurements of the delamination extension. It was, however, impossible to measure the crack length when two cracks overlapped. Visual observations on the sides of the test specimen were used to verify which crack extension was measured.

In some cases the crack front was not uniform along the specimen width (the x_3 direction). For this reason, the delamination/crack length of each crack was measured at three positions along the specimen width as shown in Fig. 4. Results for all three positions along the specimen width will be presented.

2.4. Issues with non-symmetric specimens

In general, the use of non-symmetric specimens, with the ply drops on one side only (Fig. 2), can result in a complex stress field in particular at the first ply drop (in the thin section of the specimen). However, for long specimens, such as the one depicted in Fig. 2, the bending ratio [27], in static tensile tests, is very small, less than 0.03
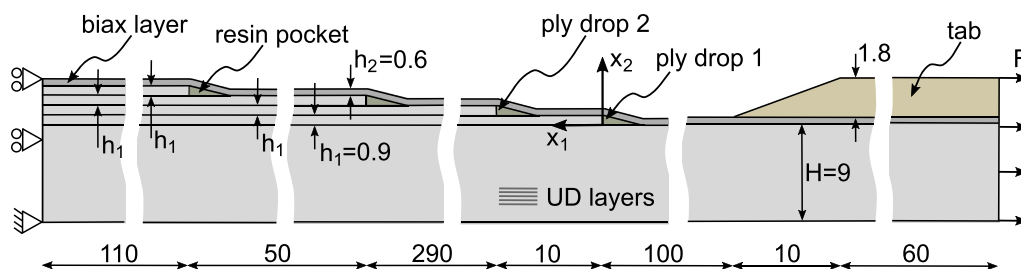

Fig. 2. Specimen dimensions and position of the ply drops (all dimensions in mm).
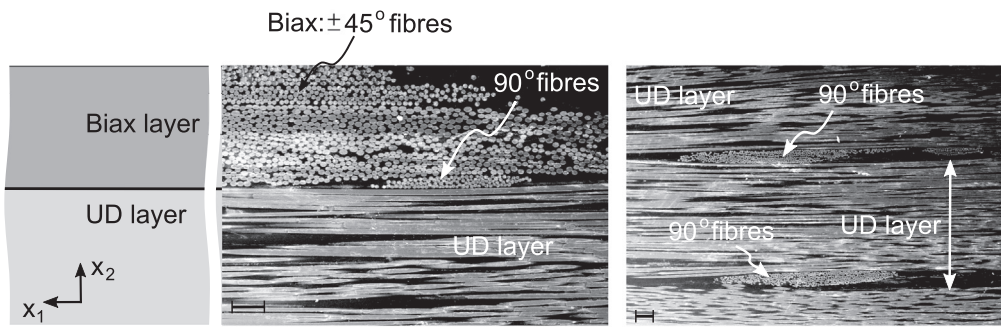
Fig. 3. Details of the 0° and ±45° plies/layers architecture showing the support threads (0°) between the reinforcing fibres (0° and ±45°). The scale bars are equal to 100 μm.
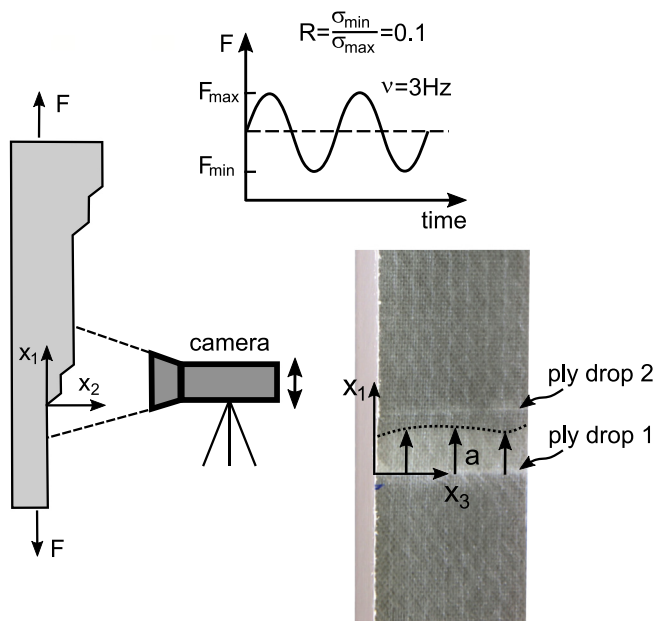

Fig. 4. Cyclic testing of the ply drop specimens with a camera used to monitor the cracks/delaminations extension with the number of cycles.

Fig. 5. Images of damage initiation: tunneling cracks and crack/delamination growth. $\sigma_{max} = 136.2$ MPa, $R = 0.1$.

[24,28] and smaller than 0.1 [29]. The bending ratio was measured by two strain gauges on the opposite faces in the thin section of the ply drop specimens. Then, the specimen can be analysed as being subjected to uniform tension. This makes the interpretation of the results easier.

3. Experimental results

3.1. Fatigue crack initiation and growth from ply drops

The damage initiation from a ply drop and the subsequent growth of cracks/ delaminations with cycles will be first shown with a series of optical images. The maximum applied stress for the specimen shown in Fig. 5 is $\sigma_{max} = 136.2$ MPa. The position of the ply drops 1 and 2 can be easily seen as lighter lines in the photo shown in Fig. 5a which was taken at $N = 1000$ cycles. At this number of cycles there is no damage in the element specimen. In Fig. 5b, recorded at 5000 cycles, a tunneling crack (a crack between the ply drop and the resin pocket, along direction x_3) denoted Tunneling Crack 1 has formed. Since the specimen was monitored/photographed at periodic intervals, it is possible to estimate the number of cycles for the initiation and growing of the tunneling crack at ply drop 1. However, since photographs were
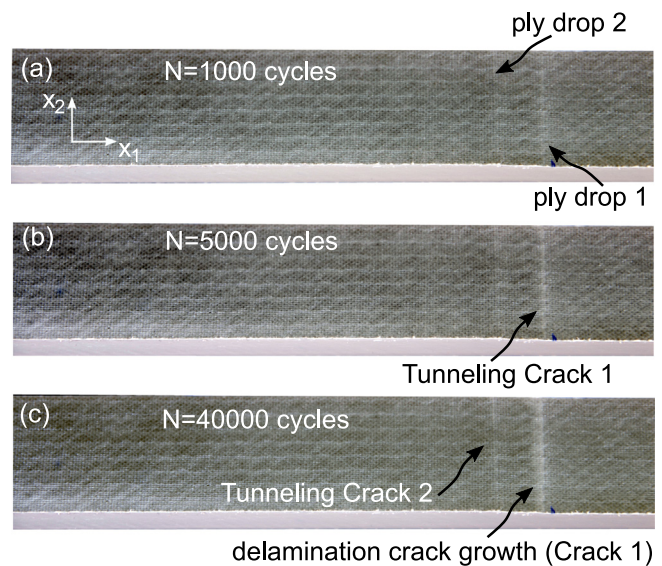
not taken for every cycle and it is not possible to exactly determine the time when the tunneling crack appears. However, once a tunneling crack initiates, it propagates fast along direction x_3.

At 40000 cycles (Fig. 5c) the second tunneling crack (denoted as Tunneling Crack 2) has formed. A delamination crack between ply drop 1 and the composite beam (denoted Crack 1) has initiated from the tunneling crack (Fig. 5b) and has started to propagate in the x_1 direction. The delamination crack plane has been confirmed by observations of the specimen at the $x_1 - x_2$ plane. This finding is in agreement with experimental observations elsewhere [8].

Fig. 6 shows the specimen at 100000 cycles. A new delamination crack (Crack 2) has now formed at Tunneling Crack 2. At $N = 100000$ cycles (Fig. 6a) a clear increase in the length of the Crack 1 can be observed when compared with the crack length at $N = 40000$ cycles (see Fig. 5c). No delamination is observed at ply drop 2 and the resin pocket yet.

At $N = 200000$ cycles (Fig. 6b), the front of Crack 1 approaches ply drop 2 (at $x_1 = 10$ mm). Crack 2 has grown by a small amount. Crack 1 reaches ply drop 2 at $N \approx 370000$ cycles (Fig. 6c).

At $N = 400000$ cycles (Fig. 7a) both Crack 1 and Crack 2 grow in the x_1 direction. At this stage, it is only possible to measure the extension crack delamination 2. Since the crack tip of Crack 1 1 lies below Crack 2, Crack 1 is not optically visible in the $x_1 - x_3$ plane. When the number of cycles has increased to $N = 450000$ (Fig. 7b), Crack 2 stops
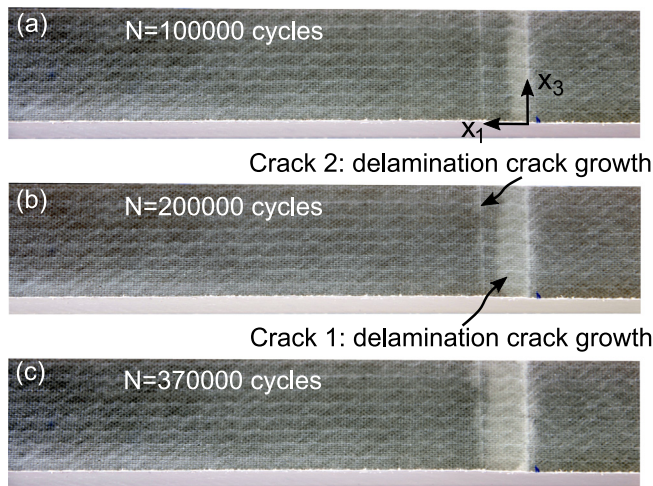
Fig. 6. Images of damage evolution of Crack 1 and Crack 2: crack/delamination growth. $\sigma_{max} = 136.2$ MPa, $R = 0.1$.
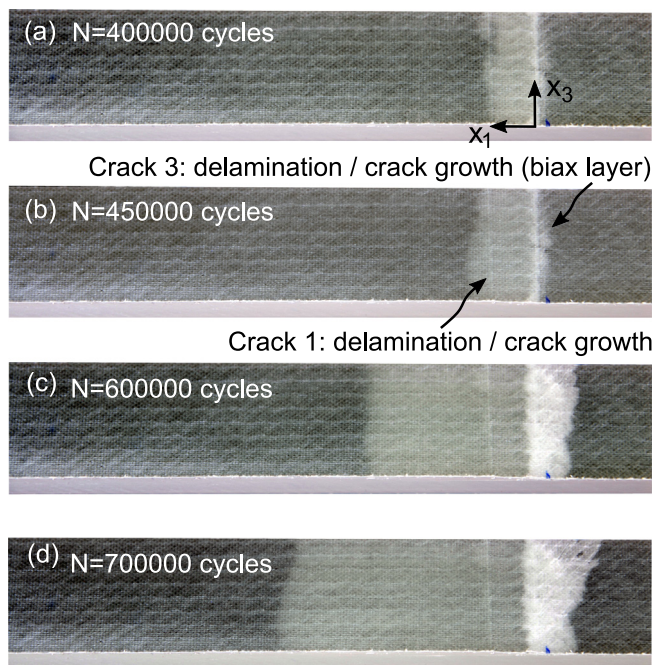

Fig. 7. Images of damage evolution beyond the second ply drop: Only Crack 1 and Crack 3 grow. $\sigma_{max} = 136.2$ MPa, $R = 0.1$.

growing and Crack 1 now grows ahead of Crack 2 and therefore becomes visible. Then, it becomes possible to measure the crack/delamination 1 growth again. At this number of cycles, a crack between the biax layer and the resin pocket, denoted Crack 3, appears and propagates in the negative x_1 direction.

The further growth of these two cracks/ delaminations, Crack 1 and Crack 3, can be observed in Fig. 7c for $N = 600000$ cycles and in Fig. 7d for $N = 700000$ cycles. Crack 1 continues to increase in length until it reaches the other end of the element specimen. The other delamination crack, Crack 3, grows away from the resin pocket (in the negative x_1 direction) and continuous growing between the biax layer the composite beam but later stops to grow as the biax layer fails in a damage zone of multiple tunneling cracks in both the $+45°$ and $-45°$ directions.

The same sequence of damage mechanisms was observed for other σ_{max} values, with the only difference being the number of cycles where a certain damage mechanism occurred.

3.2. Quantitative crack length evolution

Figs. 8–10 show the cracks/ delaminations extension as a function of the number of cycles, measured from images similar to Figs. 5,6 for three different levels of σ_{max}: In Fig. 8 for $\sigma_{max} = 130.6$ MPa, in Fig. 9 for $\sigma_{max} = 136.2$ MPa and in Fig. 10 for $\sigma_{max} = 141.8$ MPa. In these figures, the horizontal axis represents the number of cycles and the vertical axis the crack tip position (normalised with the unidirectional ply thickness, $h_1 = 0.9$ mm) of each delamination crack. The position of the ply drops 1 and 2 are also indicated in the vertical axis. For all specimens, the nominal distance between ply drops 1 and 2 is 10 mm (see Section 2.2) and the origin of the x_1 coordinate system is taken at the position of ply drop 1. The positive x_1 direction is towards ply drop 2. As mentioned, each crack length is measured in three position along direction x_3 (see Section 2.3).

Fig. 8 shows that Crack 1 propagates fast for the first ≈ 200000 cycles (crack length $x_c/h_1 \approx 5$, where x_c is the x_1 coordinate of the tip of each crack) and then the crack growth rate decreases to a near-constant value for $N > 300000$ cycles. Tunneling Crack 2 also appears relatively early but a delamination initiated at this location (Crack 2) does not grow or grows very slowly initially (in many cases, it was not possible to measure this crack extension in the early stages due to the image resolution limits). Once Crack 1 passes the tip of Crack 2, Crack 2 stops to further grow for the remaining of the test, while the crack growth rate of Crack 1 increases. Once Crack 1 is away from the position of the tip of Crack 2 (at a distance larger than H), it attains a constant growth rate significantly higher than earlier in the thinner section (between ply drops 1 and 2). The crack growth rate of Crack 3 (the debond crack between the biax layer and the resin pocket) is relatively low in comparison with the growth rate of the main delamination (Crack 1). For $N \approx 1300000$, Crack 3 grows a bit faster as it propagates between the biax layer and the composite beam. The $\pm 45°$ plies fail at some point (N approximately larger than 1800000) and then Crack 3 stops growing.

Fig. 9 is a plot similar to Fig. 8 for σ_{max} equal to 136.2 MPa. The sequence of damage mechanisms and the growth rates with cycles of the different delaminations are qualitatively identical to Fig. 8 for $\sigma_{max} = 130.6$ MPa. Due to the higher σ_{max}, the damage mechanisms appear at smaller number of cycles. For instance, the first tunneling crack appears at approximately 1500 cycles, i.e. at a lower number of cycles than the approximately 6000 cycles for $\sigma_{max} = 130.6$ MPa (Fig. 8). The second tunneling crack also is formed earlier, at $N \approx 15000$, earlier than $N \approx 30000$ for $\sigma_{max} = 130.6$ MPa.
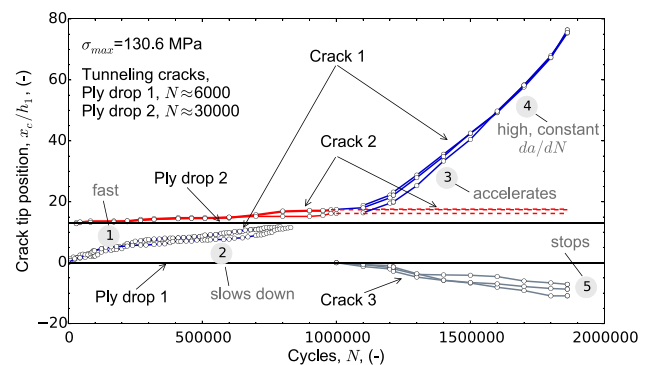

Fig. 8. Crack tip position normalised with respect to the ply drop 1 position (along direction x_1), of the different cracks is shown as a function of the number of cycles, N, for $\sigma_{max} = 130.6$ MPa. Crack 1: delamination between ply drop layer 1 and composite beam, Crack 2: delamination between ply drop layers 1 and 2 and Crack 3: initially delamination between the biax layer and the resin pocket and later between the biax layer and the composite beam.
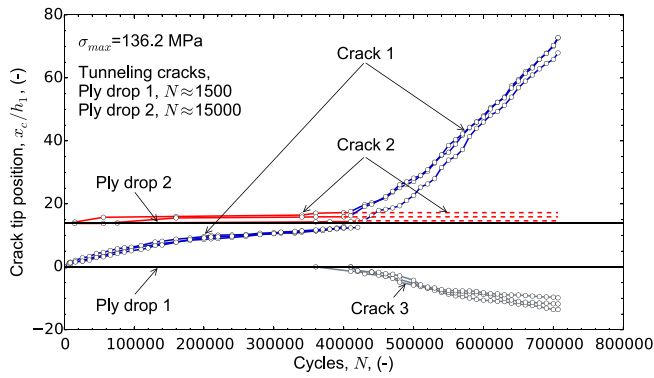
Fig. 9. Crack tip position normalised with respect to the ply drop 1 position (along direction x_1), of the different cracks is shown as a function of the number of cycles, N, for $\sigma_{max} = 136.2$ MPa. Crack 1: delamination between ply drop layer 1 and composite beam, Crack 2: delamination between ply drop layers 1 and 2 and Crack 3: initially delamination between the biax layer and the resin pocket and later between the biax layer and the composite beam.

Fig. 10. Crack tip position normalised with respect to the ply drop 1 position (along direction x_1), of the different cracks is shown as a function of the number of cycles, N, for $\sigma_{max} = 141.8$ MPa. Crack 1: delamination between ply drop layer 1 and composite beam, Crack 2: delamination between ply drop layers 1 and 2 and Crack 3: initially delamination between the biax layer and the resin pocket and later between the biax layer and the composite beam.
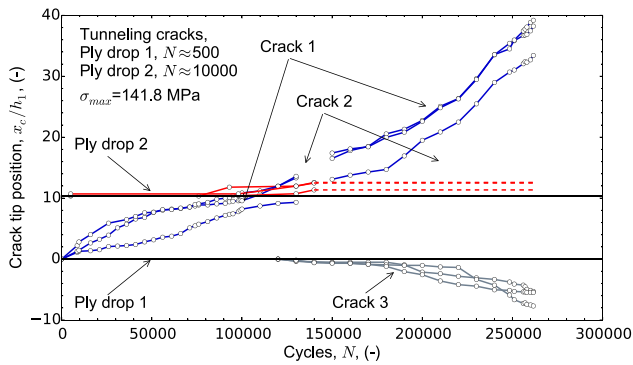
Likewise, for $\sigma_{max} = 136.2$ MPa, the growth rate of the main delamination, Crack 1, is much larger when the delamination propagates in the thick section (beyond ply drop 2) than when it propagated in the thin section between ply drops 1 and 2, see Fig. 9.

Fig. 10 shows the measurement of the delaminations lengths with cycles for σ_{max} equal to 141.8 MPa. The overall damage sequence is identical to the previous cases shown in Figs. 8 and 9 but the damages evolves faster. The first tunneling crack is visible almost from the beginning of the test at $N \approx 500$ cycles. The second tunneling crack is formed at $N \approx 10000$ cycles which is smaller than $N \approx 15000$ cycles for $\sigma_{max} = 130.6$ MPa (Fig. 9).

For this specimen, the crack length along direction x_3 of Crack 1 is not uniform (see Section 2.2) in the initial stages of the test when the crack is between ply drops 1 and 2. However, this initial non uniform crack/delamination crack growth does not change the overall results.

3.3. Crack growth rates

In Fig. 11 the early stages of the delamination Crack 1 growth (from ply-drop 1 to ply-drop 2) with cycles is plotted for the three different σ_{max} values. For each crack, only one crack length measurement along the width of the specimen (Section 2.3) is plotted. For all σ_{max} values, the growth rate decreases significantly and approaches a constant

value as the crack approaches ply drop 2. For $\sigma_{max} = 130.6$ MPa, the crack extension rate is initially 0.017 μm/cycle up to ≈ 300000 cycles and then decreases to about 0.009 μm/cycle until the crack reaches ply drop 2.

For $\sigma_{max} = 141.8$ MPa, the crack growth rate in both regions is more than 4 times larger than the corresponding extension rate for $\sigma_{max} = 130.7$ MPa. This illustrates that the cyclic stress levels have a strong influence on the crack extension between ply drop 1 and ply drop 2. It can be noted that for all three cases the constant growth rate is attained for $x_c/h_1 > 6$–7.

Fig. 12 shows the crack tip position of Crack 1 beyond ply drop 2 i.e. between ply drop 2 and ply drop 3 (see Fig. 2). In Fig. 12, the ply drop 2 is at $x_c/h_1 = (x_1 - d)/h_1$. Once the crack tip position is about 10 times the ply thickness, the crack growth rate becomes constant e.g. independent of the crack tip position.

By comparing the crack growth rates of the first region of Fig. 11 with the crack growth rates of Fig. 12, it can be seen that for $\sigma_{max} = 130.6$ MPa and $\sigma_{max} = 136.2$ MPa the crack growth rate beyond ply drop 2 (thick section) is about 8 to 10 times larger than the crack growth rate in the constant crack growth region of Fig. 11. For $\sigma_{max} = 141.8$ MPa, the crack growth rate in the thick section is approximately 4 times the crack growth rate in the constant crack growth region of Fig. 11.

In another study [28] it has been found, for exactly similar specimens, that under static loading the propagation of the delamination
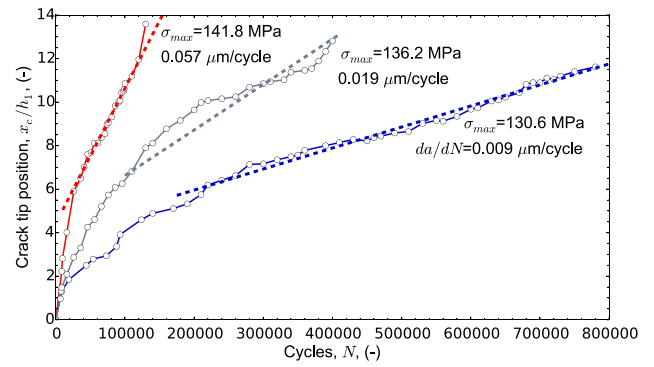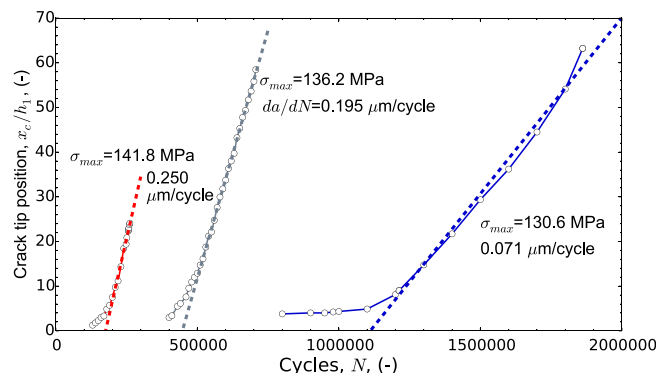

Fig. 11. Delamination length of Crack 1 between ply drop layer 1 and the composite beam, as a function of the number of cycles until Crack 1 reaches ply drop 2 region. The position of ply drop 1 is at $x_c/h_1 = 0$. The crack length data for each applied stress correspond to measurements at one position across the specimen width.

Fig. 12. Delamination, between ply drop layer 1 and the composite beam, growth per cycle for different σ_{max} from ply drop 2 to a distance away from ply drop 2. The position of ply drop 2 is at $\tilde{x}_1/h_1 = (x_1 - d)/h_1$. The crack length data for each applied stress correspond to measurements at one position across the specimen width.

crack between ply drop 1 and the composite beam, Crack 1, occurs at stress levels between 200 and 250 MPa. The present measurements, for example Fig. 12, are in agreement with the results of that study [28], where the delamination grows in the thick section between ply drops 2 and 3, between a rate of approximately 0.01 μm per cycle for σ_{max} = 110 MPa and approximately 7.0 μm per cycle for σ_{max} = 180 MPa. The crack growth rate, see Figs. 11 and 12 increases significantly with a relatively small increase of σ_{max}. Similar results were reported by Agastra et al. [4] for a crack between ply drop 1 and the composite beam.

3.4. Summary of experimental observations

The damage sequence observed experimentally, through observations during the tests and scanning electron microscopy examinations after the tests, is shown schematically in Fig. 13. The tunneling crack between ply drop 1 and the resin pocket (Tunneling Crack 1) is the first damage (Fig. 13a). Once it has formed, it propagates relative fast across the specimen width. Then, a delamination, Crack 1, initiates from the bottom of the tunneling crack and propagates along the interface between ply drop 1 layer and the composite beam and later a secondary delamination between ply drop layer 1 and the biax layer, Crack 1a (Fig. 13b) initiates from the top of the tunneling crack.

Then, Tunneling Crack 2 forms (Fig. 13c), while the two previous delaminations, Crack 1 and Crack 1a, continue to grow. Crack 1 has a higher growth rate than Crack 1a that (later) stops growing.

Next as shown in Fig. 13d, delaminations are initiated from the top and bottom of Tunneling Crack 2, one between ply drop layer 1 and 2, denoted Crack 2, and one between ply drop layer 2 and the biax layer,

Crack 2a. About the same time as Crack 1 approaches ply drop 2, the secondary delamination, Crack 1a, stops to grow along the interface.

When the tip of the main delamination, Crack 1, extends beyond the tip of Crack 2 (Fig. 13e) the growth rate of Crack 1 increases to a higher, constant value, while Crack 2 grows at a much lower rate. Crack 2a grows at an even lower rate. It should be noted that due to the fabric structure, a clear weak interface exists between the 0° layers (see Fig. 3) and and thus Crack 1a propagates along this interface in the x_1 direction between 0° layers. On the other hand, the structure of the biax layer creates additional weak paths, between the ±45° fibre bundles, where a crack can grow (see Fig. 13e). Next, Crack 1a kinks into the biax layer, which essentially breaks up. Once the biax layer has broken (Fig. 13e), Crack 1 continuous to grow in a steady-state situation where the layers above the crack plane (Crack 1) become stress-free as the crack tip advances. At the same time, Crack 3 initiates from the upper tip of the tunneling crack of ply drop 1 and grows in the negative x_1 direction along the interface between the biax layer and the resin pocket, Crack 3 (Fig. 13e).

When Crack 1 is away from ply drop 2 (see Fig. 13f) it grows at a higher rate which attains a constant value while Crack 2 and Crack 2a completely stop growing. In some cases Crack 2a kinks into the biax layer and then stops to grow, similarly to the crack shown in Fig. 13e propagating into the biax layer. The crack between the biax layer and the resin pocket, Crack 3, propagates along the interface of the end of the resin pocket (in the negative x_1 direction) and then becomes a delamination crack propagating between the biax layer and the composite beam. At this point, as indicated in Fig. 13g, only two cracks continue to grow: Crack 1 that grows at a fast constant growth rate and Crack 3. Then, Crack 3 kinks into the ±45° and thus
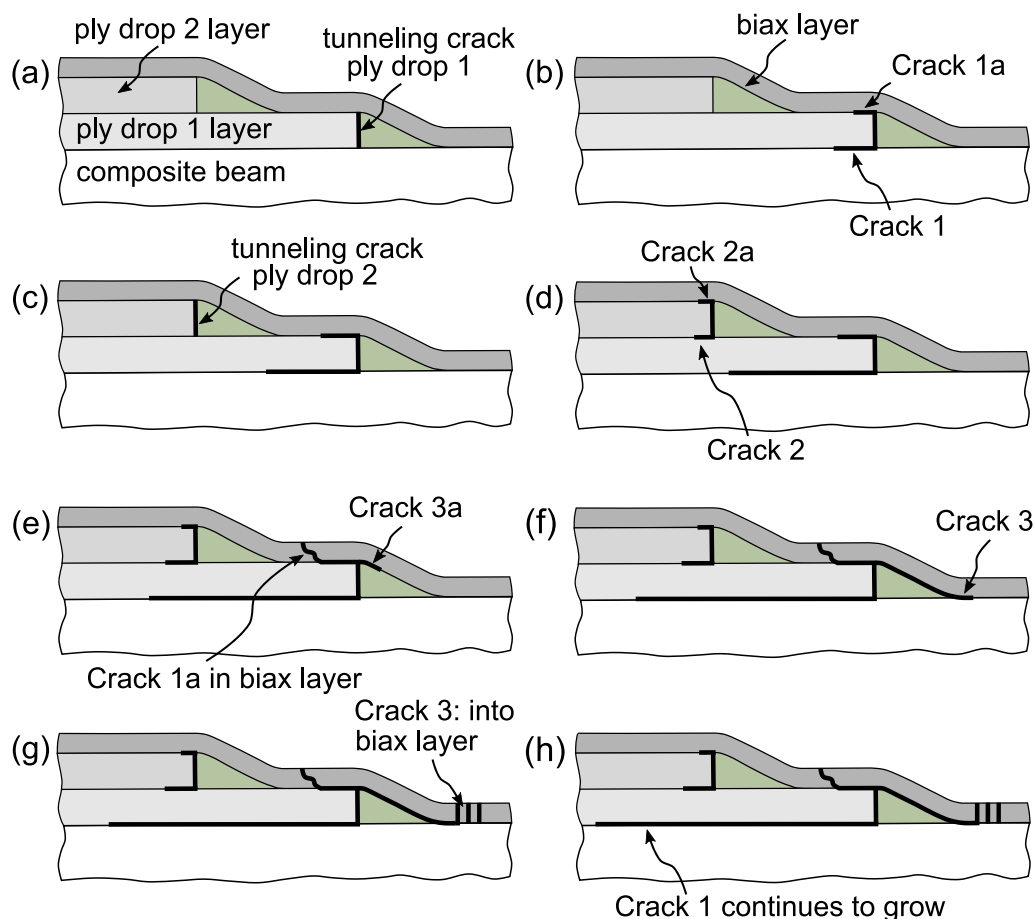

Fig. 13. Schematic drawing of the damage sequence in the element specimen with ply drops.

stops to further grow. Finally (Fig. 13h) only Crack 1 grows. It was possible to grow this delamination at a constant growth rate for several centimeters as shown in Fig. 12. It is remarkable that the somewhat complicated damage evolution at ply-drops ends in a situation where only one crack propagates at a constant rate. This suggests that this part of the problem can be analysed as a steady-state problem, which greatly simplifies the analysis e.g. as can be seen from Fig. 12, for all σ_{max} the Crack 1 growth rate attains a constant value when its crack tip is at some distance away from ply drop 2 (approximately larger than H).

4. Numerical models

In order to get a deeper understanding of the experimental findings, the finite element method was employed to model the element test of Fig. 2 as a two-dimensional plane stress problem using the commercial finite element code Abaqus, version 6.17 [30]. Two models were used. A model with cohesive zones along the interfaces (Section 4.1 and a linear elastic fracture mechanics (LEFM) model with two crack tips (Section 4.2).

4.1. Cohesive zone model for ply drop interaction

Fig. 14a shows a schematic illustration of the cohesive based finite element model to study the ply drop interaction. In accordance with the damage evolution shown in Fig. 13, cohesive zones were inserted along all interfaces, e.g. also between the UD plies the resin pockets. The tunneling cracks were assumed to pre-exist; in the model the ends of the ply drops are fully debonded from the resin pockets. Certain cracks as it will be discussed in Section 3 are tunneling cracks in the off-axis plies, i.e. Crack 3. It is expected that a 2D cohesive zone representation of the off-axis cracks is not accurate in particular with respect to their out-of-plane growth. However, for the purpose of the current work, the modelling of the off-axis tunneling cracks with 2D cohesive elements can give information if these cracks will initiate or not and comparisons can be made with the experimental observations.

With reference to Fig. 14, the nodes at the left hand side of the specimen, at $x_1 = 260$ mm, were constrained in the x_1 direction and the bottom corner node also in the x_2 direction. Displacements in the x_1 direction were prescribed incrementally to the nodes at $x_1 = -150$ mm. Thus, not the entire length of the specimen of Fig. 2 was modelled e.g. the length in the model was smaller than the real specimen but long enough to ensure that there was no influence from the boundary conditions. Furthermore, only the two closed distance ply drops were modelled. The distance, d, between the two tunneling cracks (or the two ply drops) was 10 mm. The thickness of the 0°-

layers, h_1, was 0.9 mm and the thickness of the biax-layer, h_2, was 0.6 mm.

The composite plies were modelled with four-node and three-node plane stress elements in order to control the mesh transition from small size elements near the cohesive zones to larger elements away from the cohesive zones as shown in Fig. 14b for Crack 1 and Crack 3b. The elastic constants for the composite plies (orthotropic linear-elastic solids) and the epoxy resin (isotropic linear-elastic) are given in Table 1. E_{11} was experimentally measured, whereas the other elastic constants were estimated based on micromechanics and the fibre and resin properties [31].

The Abaqus linear four-noded cohesive elements were used to model the cohesive zones and the cohesive element length was equal to $0.02h_1$. As can be seen from Fig. 14b the cohesive elements had a finite thickness, equal to $0.0075h_1$ to avoid element interpenetration [32,33]. It was ensured that a large number of cohesive elements (more than 50) were active in the cohesive zone during the loading stage, which is significantly higher than the minimum number (4–8) suggested by Turon et al. [34] and references therein. The traction-separation law, uncoupled mixed mode cohesive law with linear softening [35,33], was implemented in an user material Abaqus Fortran subroutine to ensure a path independent mixed mode fracture energy [36,37]. The cohesive law properties assumed are given in Table 2. In the present work, the mode II cohesive law is identical to the mode I cohesive law. The normal and shear peak tractions are denoted as $\hat{\sigma}_n$ and $\hat{\sigma}_t$, the corresponding critical separations as δ_{no} and δ_{to}, and the mode I and mode II fracture energies as Γ_n and Γ_t. The same cohesive law parameters were used for all cracks. Finite element simulations were also performed with other cohesive law parameters than those listed in Table 2, and for different cohesive laws for the different cracks of Fig. 14a. The use of different cohesive law properties will be discussed in Section 5.

In order to overcome convergence difficulties that are typically encountered in FE simulations with implicit solvers [38] and in particular in the presence of more than one crack [33], an explicit solver was used. Therefore, in order to obtain a quasi-static solution, the mass-scaling approach [30,39] was used. In all simulations, it was ensured that the kinetic energy and the energy dissipated by viscosity (viscous damping is always included in Abaqus/Explicit) were negligible, below 0.5% of the strain energy.

4.2. Linear elastic fracture mechanics model for steady-state crack growth

Fig. 15a shows the finite element model used to calculate the energy release rate, $\mathscr{G}$, of Crack 1 and Crack 2, representing the cases where Crack 1 has grown away from the first ply drop region e.g. $a_1 > 0$ and the x_1 coordinate of the tip of Crack 1 is smaller, equal or larger
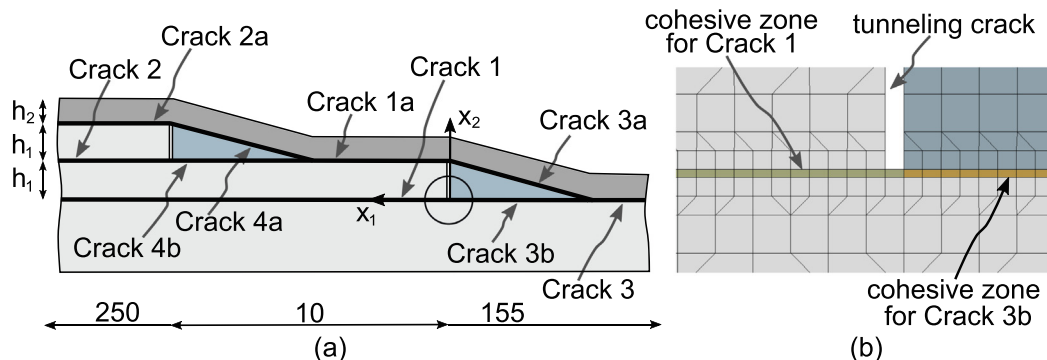

Fig. 14. a) Schematic illustration of the cohesive based finite element model showing all the cohesive zones where cracks can initiate and grow and b) detailed view of the finite element mesh at $x_1 = 0, x_2 = 0$ showing the finite thickness cohesive elements to model cohesive zones for Crack 1 and Crack 3b. All dimensions in mm and the resin pocket angle is 14°.

Table 1
Elastic constants of the epoxy resin and of the unidirectional (UD) and biaxial plies.

	E_{11} (GPa)	E_{22} (GPa)	ν_{12} (–)	G_{12} (GPa)	G_{13} (GPa)	G_{23} (GPa)
UD	38.000	11.600	0.284	3.460	4.460	3.460
Biaxial	10.593	10.593	0.531	8.640	4.074	8.640
	E (GPa)	ν (–)				
Epoxy	3.500	0.350				

Table 2
Parameters of mode I and mode II traction-separation laws for all cohesive zones.

Mode I			Mode II		
$\hat{\sigma}_n$ (MPa)	δ_{no} (mm)	Γ_n (J/m²)	$\hat{\sigma}_t$ (MPa)	δ_{to} (mm)	Γ_t (J/m²)
20.00	0.01	1000.00	20.00	0.01	1000.00

that the tip of Crack 2. The length of Crack 2, a_2, is kept constant and equal to 2.22 h_1. All the other cracks are modelled as fully delaminated in the LEFM models. A focused mesh for the LEFM models, as shown in Fig. 15b, was used close to the crack tip of both cracks in order to calculate the crack energy release rate based on J integral evaluation as implemented in the Abaqus code [30]. The size of the smallest crack tip element was 0.0015 h_1.

In order to compute the energy release rate from static finite element solutions, a series of finite element simulations were run with increasing the Crack 1 length a_1 (the x_1 coordinate of the crack tip of Crack 1), while keeping the length of Crack 2 constant, $a_2/h_1 =$ 2.22. More elaborated analyses, i.e. by simultaneously increasing the length of Crack 2, could be also tested. However, to analyse the experimental findings, it is preferred to use a simple model.

5. Numerical results

5.1. Results for cohesive zone modelling

Fig. 16 shows the finite element predictions of the crack tip positions under a monotonically increasing end-displacement, predicted using the cohesive zone model of Fig. 14a. The results of Fig. 16 can be qualitatively compared with the cyclic crack growth results of Figs. 8–10. If the crack length increases under increasing displacement, then a corresponding cyclically loaded specimen would undergo a faster cyclic crack growth (have a higher crack growth rate). The main delamination, Crack 1, grows much longer in an unstable fashion once it extends beyond the tip of Crack 2. At the final stage, the crack growth rate of Crack 1 is very fast; a consequence of static finite element solution, which at some point becomes unstable. Qualitative, the interplay between Crack 1 and Crack 2 in Figs. 8–10 is the same.
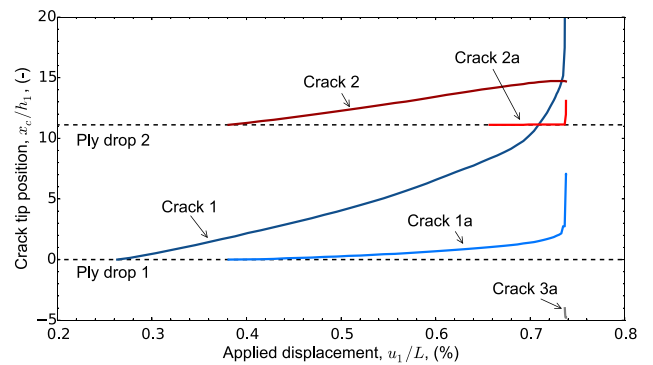

Fig. 16. Finite element results for the normalised crack tip position, with respect to the ply drop 1 position (along direction x_1), of the different cracks/delaminations (defined in Fig. 14a) as a function of applied displacement, u_1, along x_1.

The predicted response for Crack 2 also agrees qualitatively with the experimental observations e.g. Crack 2 initiates later than Crack 1, it propagates less than Crack 1 and more importantly it arrests as the crack tip of Crack 1 passes by. Crack 1a initiates later than Crack 1 but it grows very slow except for high applied displacements, which is the range where the static simulations become unstable. Crack 3b and Crack 4b do not initiate at all and Crack 3a initiates approximately when Crack 2 arrests. Its growth rate is relatively fast but the crack initiates at the end of the simulation shortly before the simulation turns unstable.

The same trends where found for other cohesive law parameters than those listed in Table 2, with the main difference being that cracks
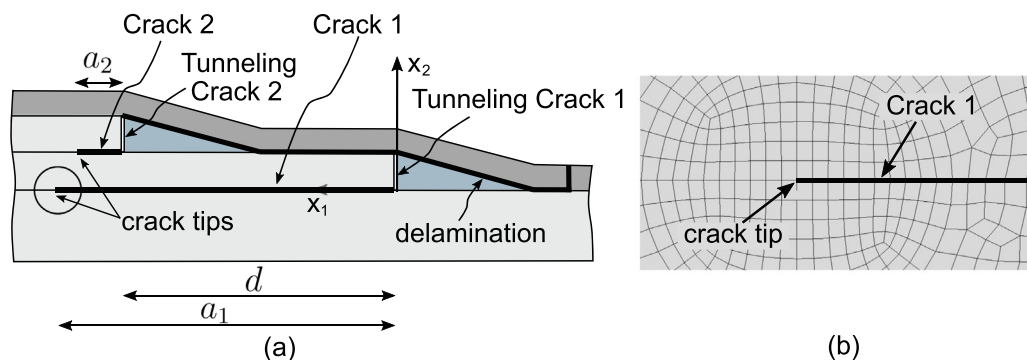

Fig. 15. a) Schematic illustration of the LEFM based finite element model showing the two cracks tips (cracks 1 and 2 in Fig. 14) and a fully developed delamination at the wake for Crack 1 and Crack 2, b) detailed view of the finite element mesh at the. tip of Crack 1.

would initiate at different applied displacement. In addition, few simulations were performed with using different cohesive laws for the different cracks but qualitatively the results were similar to the results of Fig. 16.

5.2. Results using linear elastic fracture mechanics

Fig. 17 shows the LEFM results in terms of the energy release rate for Crack 1 and Crack 2 when both crack tips have the same x_1 coordinate and when Crack 1 extends beyond or ahead of the tip of Crack 2, which is held stationary. As described in Section 4.2, Fig. 17 is constructed by a series of static finite element simulations. It can be seen that when the tip of Crack 1 has grown well beyond the tip of Crack 2 ($a_1 > 15h_1$), the energy release rate of Crack 1 is significantly higher than the energy release rate of Crack 2 and it is fairly constant indicating steady-state crack growth in accordance with the experimental results of Fig. 12. For these cases, the energy release rate for Crack 2 is nearly zero. This suggests that Crack 2 would arrest. This prediction agrees with the experimental observations of Section 3. It should be mentioned that the results of Fig. 17 are also in qualitative agreement with the finite element results of Goutianos and Sørensen [24] who used a simplified geometry consisting of one ply drop. The mode mixity, $\psi = \tan^{-1}(K_{II}/K_I)$, is $-37.0°$ for $a_1/h_1 = 20$ and increases to $-41.1°$ for $a_1/h_1 = 40$. The negative sign of ψ (and K_{II}) indicate that the crack tends to kink downwards into the thick composite beam (see Fig. 15 for the crack tip direction).

When Crack 1 is very long, the steady-state energy release rate can be calculated analytically by extending the model of Sørensen [40], as briefly presented in A. With $H = 10h_1$, the layer thicknesses given in Fig. 2, and the values of E_{11} listed in Table 1, Eq. A-1 becomes:

$$G_{ss} = 0.898 \frac{\bar{\sigma}_o^2 h_1}{E_{11}} \tag{1}$$

The analytically calculated normalised energy release rate, as predicted by Eq. 1, is then equal to 0.898, about 4% lower than the energy release rate calculated for a_1 equal to $40h_1$ using the finite element model (see Fig. 17). Thus, it can be argued that the analytical model is fairly accurate and it could be used to efficiently calculate cyclic crack rates as described elsewhere [40].

6. Discussion

6.1. Distance between ply drops

The distance between ply drops 1 and 2 was chosen as 10 mm to study the interaction between closely spaced ply-drops (see Sec-
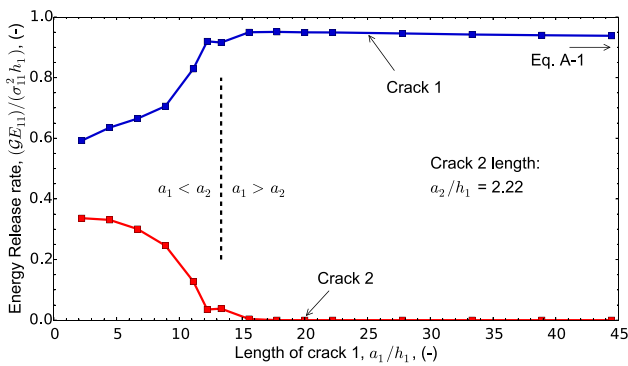
tion 2.2). It was found experimentally that this distance might be a bit too small and crack interaction prevents Crack 1 from reaching a near-constant crack growth rate when approaching ply drop 2. A larger distance between ply drops 1 and 2 is recommended for future work.

6.2. On steady-state cracking

Using linear elastic fracture mechanics models made by the finite element method, Goutianos and Sørensen [24] found for a similar specimen that the energy release rate increases from a low value to constant value (steady state) when the crack length is larger than the thickness of the specimen with a single ply drop. This, a constant steady-state energy release rate, is consistent with the observations of a near-constant crack growth rate of the present work. For the specimen tested in the present study, the near-constant growth rate observed for Crack 1 approaching ply drop 2 indicates a near-steady-state situation. However, a true steady-state requires that the biax layer is broken (see Fig. 13e) so that the delaminated layers become stress-free. It is presently unclear why the crack growth rate decreases in the earlier stages of delamination. An increasing fibre bridging zone (not modelled) would unload the crack tip. On the other hand, the distance between ply drops 2 and 3 is much larger than the thickness of the element specimen and thus the crack growth rate can reach a constant crack growth rate when the crack is further away from ply drop 2. As explained in the previous section, when the biax layer breaks at Crack 1a, then the problem is in steady-state (constant energy release rate independent of crack tip position). Even in the case of large-scale fibre bridging, a constant growth rate is expected under steady-state when the bridging zone is fully evolved. This follows from an application of the J integral. But the LEFM results of Fig. 17 show that the energy release rate of Crack 1 increases as it extends from ply drop 1 towards ply drop 2. A decreasing crack growth rate while the energy release rate is increasing suggests that the interface exhibits an increase in fracture resistance with increasing crack extension. Increase in fracture resistance by fibre bridging has been documented under static mixed mode delamination [41]. Under cyclic loading, the presence of large-scale bridging causes the crack growth rate to decrease significantly [42].

6.3. Description of cyclic crack growth rate by the Paris-Erdogan Law

As discussed in Sections 3.4 and 5.2 when Crack 1 grows away from ply drop 2 it grows at a constant rate. The analytical solution of A, to predict the steady-state energy release at the tip of crack, can be used to calculate the magnitude of the stress intensity factor range, $|\Delta K|$ (see B for details). Then, the crack growth rate as a function of $|\Delta K|$ can be plotted as it is shown in Fig. 18. Crack growth data from a parallel study using exactly identical specimens [28] study are included.

To calculate $|\Delta K|$, it is assumed that LEFM is applicable to describe the fracture process i.e. there is no fibre bridging or friction at the wake of the crack tip and that plastic deformation is zero or close to zero. Furthermore, since both the first ply and the composite beam are made of UD layers, $E_o = E_{11}$ of the UD layer (see Table 1). Then, the steady-state energy release rate $\mathscr{G}_{ss}$, from Eq. 1, is related to $|\Delta K|$ through Irwin's relation:

$$\mathscr{G}_{ss} = \frac{K_I^2 + K_{II}^2}{E_o} = \frac{|K|^2}{E_o}. \tag{2}$$

For cyclic loading, the corresponding relation between $|\Delta K|$ and G_{max} becomes (B):

$$|\Delta K| = \sqrt{G_{max}E_o}(1 - R) = 0.947\sqrt{h_1}(1 - R)\bar{\sigma}_{max} \tag{3}$$

where G_{max} has been expressed in terms of σ_{max} by the use of Eq. 1 and thus $|\Delta K|$ can be calculated from σ_{max}.

Fig. 17. Finite element results of the normalised energy release rate, $\mathscr{G}$, for Crack 1 and Crack 2 (see Fig. 15a), as a function Crack 1 length. The length of Crack 2 is held constant. σ_{11} is the stress in the composite beam at the right end of the model in accordance with the analytical model of A.
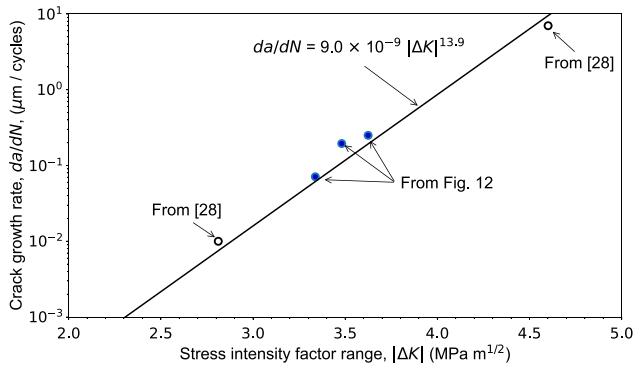
Fig. 18. Crack growth rate, da/dN, as a function of the applied stress intensity factor range, $|\Delta K|$.

The data of Fig. 18 follow a straight line. This is in accordance with the Paris-Erdogan law [43]. Normally, such Paris-Erdogan law data would be established by coupon testing, e.g. by applying cyclic loads to a mixed mode specimens such that the crack tip would be subjected to the mode mixity similar to that of a ply drop (for the present problem about $-41°$, see Section 5.2). Such data would then be used to predict the cyclic crack growth rate of the delamination crack of the ply drop. It is encouraging that the crack growth rates of the ply drop investigated in the present study (Fig. 18: da/dN - $|\Delta K|$) is consistent with a Paris-Erdogan law.

6.4. Suppression of damage evolution

The main result of the present work is the experimental measurement of the crack crack growth rate of the crack between ply drop 1 and the composite beam, Crack 1, and its change as the crack moves from the thin to the thick section of the element specimen. The initial tunneling cracks are probably difficult to suppress even when chamfered ply drops are used. However, these tunneling cracks are not critical for the integrity of a composite structure nor do they result in a significant loss of stiffness. The tunneling cracks lead to subsequent delaminations which grow and then are suppressed after certain number of cycles except for one, Crack 1, the crack between ply drop 1 and the composite beam. Modifying the interlaminar properties of the interface between the first ply and the composite beam, e.g. increasing the interlaminar fracture resistance, could result in a slower increase of the crack length with cycles. However, as the crack moves into thicker sections, its growth rate will increase at each thickness change. Thus, it is important to take into account the geometry effects when estimating the cycles for the crack to reach a certain length. A design criterion could be to prevent a delamination to reach the next ply drop.

Crack 1 is a mixed mode crack likely with fibre bridging and friction contributing to the interlaminar fracture resistance. It will be relevant and interesting to investigate the dependence of fibre bridging and friction on the crack growth rate.

7. Concluding Remarks

An element specimen with several ply drops can provide insight into the damage evolution initiated from ply drops under cyclic loading. The presence of ply drops leads to several cracks due to the material and geometry discontinuities. Among the different cracks, one delamination crack is identified as critical, the other cracks found eventually to arrest. It is shown that the crack growth rate of this critical crack depends both on the maximum applied stress under cyclic tension–tension stress fatigue and on the thickness the structure. As material thickness increases above the crack plane, the crack growth

rate increases significantly. These experimental observations were understood by finite element analyses based on cohesive zone modelling and linear elastic fracture mechanics. The experimental findings have important implications in practice, since the delamination growth rate increases to a higher value as the crack tip moves past the next ply drop to thicker sections of a composite structure or component. Designs based on damage tolerance concept, which allow cracks in a structure, can be non-conservative if the growth rate dependence on thickness transitions are not taken into account. To overcome the increasing crack growth rate as the crack moves to thicker sections of the structure, more damage tolerant composite materials could be used, utilising toughening mechanisms such as fibre bridging to decrease or even suppress crack growth.

Declaration of Competing Interest

Appendix A. Analytical solution of for the energy release rate at a ply drop of a five-layer specimen

Sørensen [40] recently presented an analytical model, based on J integral, to calculate the energy release rate at the tip of the long delamination crack initiating from a ply drop. The analysis was presented for a symmetric tri-layer specimen consisting of a central layer and two surface layers. The model of Sørensen [40] can be extended to a five-layer specimen as shown in Fig. 19 which is similar to the element test specimen used in the present work (Fig. 1).

Following the work of Sørensen [40], the steady-state energy release rate $\mathscr{G}_{ss}$ is equal to the J integral evaluated along the external boundaries, under plane stress condition:

$$\mathscr{G}_{ss} = J_{ext} = \frac{\bar{\sigma}_o^2 H}{E_o} \left(\frac{\Sigma_1 \eta_1 + \Sigma_2 \eta_2}{1 + 2(\Sigma_1 \eta_1 + \Sigma_2 \eta_2)} \right) \tag{A-1}$$

where

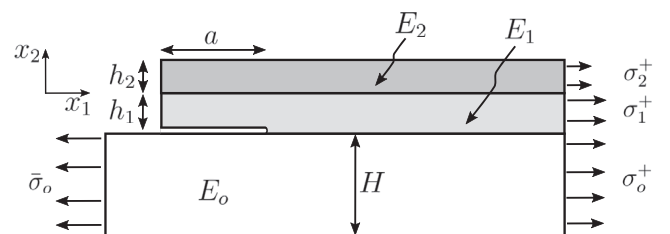$$\Sigma_1 = \frac{E_1}{E_o} \text{and} \Sigma_2 = \frac{E_2}{E_o} \tag{A-2}$$

and

Fig. 19. A five-layer specimen undergoing delamination with a shear stress τ_s in the delaminated zone. Due to symmetry only half of the specimen is shown.

$$\eta_1 = \frac{h_1}{2H} \text{ and } \eta_2 = \frac{h_2}{2H} \tag{A-3}$$

It should be mentioned that the underlying assumptions of Eq. A-1 are that all materials are orthotropic linear elastic, with E_o, E_1, and E_2 the Young's moduli in the x_1 direction (denoted E_{11} in Table 1) of the composite beam and the layers indicated in Fig. 19.

Appendix B. Mixed-mode stress intensity factor range

In this Section a relationship between the cyclic stress intensity factor range, $|\Delta K|$, and G_{max} (see A) is derived. G_{max} can be calculated from Eq. A-1 with $\bar{\sigma}_o$ equal to σ_{max}.

When the applied stress varies between the minimum and maximum values, the mode I stress intensity factor varies between a minimum and a maximum value, K_I^{min} and K_I^{max}, and the mode II stress intensity factor varies between K_{II}^{min} and K_{II}^{max} as shown in Fig. 20. Therefore, the mode I and mode II stress intensity factor ranges are:

$$\Delta K_I = K_I^{max} - K_I^{min} \text{ and } \Delta K_{II} = K_{II}^{max} - K_{II}^{min} \tag{A-4}$$

and the magnitude of the stress intensity factor range, $|\Delta K|$, for a crack subjected to mixed mode under LEFM conditions, is:

$$|\Delta K| = \sqrt{(\Delta K_I)^2 + (\Delta K_{II})^2} \tag{A-5}$$

Due to linearity, the relation between the minimum and maximum stress intensity factors in mode I and mode II is:

$$K_I^{min} = R K_I^{max} \text{ and } K_{II}^{min} = R K_{II}^{max} \tag{A-6}$$

Inserting Eq. A-6 into Eq. A-4 gives:

$$\Delta K_I = (1-R) K_I^{max} \text{ and } \Delta K_{II} = (1-R) K_{II}^{max} \tag{A-7}$$

Then, inserting Eq. A-7 into Eq. A-5 leads to:

$$|\Delta K| = \sqrt{(K_I^{max})^2 + (K_{II}^{max})^2} (1-R) \tag{A-8}$$

The Irwin's relation for mixed mode fracture (plane stress)

$$G_{max} = \frac{(K_I^{max})^2 + (K_{II}^{max})^2}{E_o} \tag{A-9}$$

can be rewritten as:

$$(K_I^{max})^2 + (K_{II}^{max})^2 = G_{max} E_o \tag{A-10}$$

Then, inserting Eq. A-10 into Eq. A-8 gives the main result, the mixed-mode stress intensity factor range in terms of G_{max}:

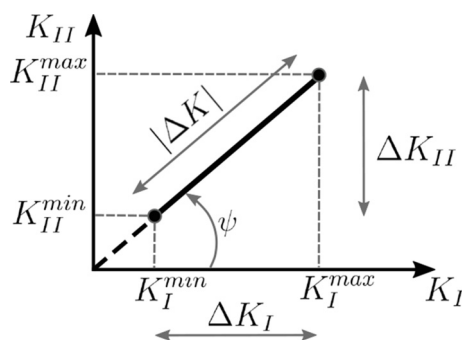$$|\Delta K| = \sqrt{G_{max} E_o} (1-R) \tag{A-11}$$

Fig. 20. Definition of mixed-mode stress intensity factor range, $|\Delta K|$.

References

[1] Gan KW, Allegri G, Hallett SR. A simplified layered beam approach for predicting ply drop delamination in thick composite laminates. Mater. Des. 2016;108:570–80.
[2] Helmy S, Hoa SV. Tensile fatigue behavior of tapered glass fiber reinforced epoxy composites containing nanoclay. Compos. Sci. Technol. 2014;102:10–9.
[3] He K, Hoa SV, Ganesan R. The study of tapered laminated composite structures: A review. Compos. Sci. Technol. 2000;60:2643–57.
[4] Agastra, P., Samborsky, D.D., Mandel, J.F.. Fatigue resistance of fiberglass laminates at thick material transitions. In: 50th AIAA/ASME/ASCE/AHS/ASC Structures, Structural Dynamics, and Materials Conference. Palm Springs, California; 2009,AIAA 2009-2411..
[5] Murri, G.B., Salpekar, S.A., O'Brien, T.K. Fatigue delamination onset prediction in tapered composite laminates. Tech. Rep. TM1016732; NASA; Langley Research Center, Hampton, Virginia 23665, USA; 1989..
[6] Fish JC, Lee SW. Delamination of tapered composite structures. Eng. Fract. Mech. 1989;34:43–54.
[7] Mandell, J.F., Samborsky, D.D., Cairns, D.S. Fatigue of composite materials and substructures for wind turbine blades. Tech. Rep. SAND2002-0771; Sandia National Laboratories; Albuquerque, NM, USA; 2002..
[8] Samborsky DD, Wilson TJ, Agastra P, Mandell JF. Delamination at thick ply drops in carbon and glass fiber laminates under fatigue loading. J. Sol.Energy Eng. 2008;130. 031001–1.
[9] Cui WC, Wisnom MR, Jones M. Effect of step spacing on delamination of tapered laminates. Compos. Sci. Technol. 1994;52:39–46.
[10] Botting AD, Vizzini AJ, Lee SW. Effect of ply-drop configuration on delamination strength of tapered composite structures. AIAA Journal 1996;34:1650–6.
[11] Khan B, Potter K, Wisnom MR. Suppression of delamination at ply drops in tapered composites by ply chamfering. J. Compos. Mater. 2006;40:157–74.
[12] Fish JC, Vizzini AJ. Tailoring concepts for improved structural performance of rotorcraft flexbeams. Compos. Eng. 1992;2:303–12.
[13] Thomas DM, Webber JPH. A design study into the delamination behavior of tapered composites. Compos. Struct. 1994;27:379–88.
[14] Thomsen OT, Rits W, Eaton DCG, Brown S. Ply drop-off effects in CFRP/honeycomb sandwich panels - Theory. Compos. Sci. Technol. 1996;56:407–22.
[15] Shim DJ, Lagace PA. Mechanisms and structural parameters affecting the interlaminar stress field in laminates with ply drop-offs. J. Compos. Mater. 2006;40:345–69.
[16] Salkepar SA, Raju IS, O'Brien TK. Strain-energy release rate analysis of delamination in a tapered laminate subjected to tension load. J. Compos. Mater. 1996;25:118–41.
[17] Vizzini AJ, Lee SW. Damage analysis of composite tapered beams. Journal of the American Helicopter Society 1995;40(2):43–9.
[18] Garg AC. Delamination - A damage mode in composite structures. Eng. Fract. Mech. 1988;29:557–84.
[19] McGowan, D.M., Ambur, D.R. Damage-tolerance characteristics of composite fuselage sandwich structures with thick facesheets. Tech. Rep. TM110303; NASA; Langley Research Center, Hampton, Virginia 23665, USA; 1997..
[20] Homan JJ. Fatigue initiation in fibre metal laminates. Int. J. Fatigue 2006;28:366–74.
[21] Alderliesten RC. Analytical prediction model for fatigue crack propagation and delamination growth in Glare. Int. J. Fatigue 2007;29:628–46.
[22] Alderliesten RC. Designing for damage tolerance in aerospace: A hybrid material technology. Mater. Des. 2015;66:421–8.
[23] McGugan M, Pereira G, Sørensen BF, Toftegaard H, Branner K. Damage tolerance and structural monitoring for wind turbine blades. Philosophical Transactions A 2015;373:20140077.
[24] Goutianos, S., Sørensen, B.F.. Fracture mechanics analysis of composites with ply-drops - measurement of delamination fatigue crack growth rate. 2018,ECCM18 - 18th European Conference on Composite Materials, 24-28 June, Athens, Greece..
[25] Lahuerta F, Koorn N, Smissaert D. Wind turbine blade trailing edge failure assessment with sub-component test on static and fatigue load conditions. Compos. Struct. 2018;204:755–66.
[26] Rueden CT, Schindelin J, Hiner MC, DeZonia BE, Walter AE, Arena ET, et al. Imagej 2: Imagej for the next generation of scientific image data. BMC Bioinformatics 2017;18:529.
[27] ASTMD3039/D3039M-17. Standard test method for tensile properties of polymer matrix composite materials. Standard; ASTM International; West Conshohocken, PA, USA; 2017..
[28] Goutianos S, Sørensen BF. Specimen for cyclic delamination crack growth rates from ply-drops. IOP Conference Series: Materials Science and Engineering 2018;388(1):012010.
[29] Bech JI, Goutianos S, Andersen TL, Torekov RK, Brøndsted P. A new static and fatigue compression test method for composites. Strain 2011;47(1):21–8.
[30] Documentation ABAQUS. United States: Dassault Systèmes Simulia Corp; 2017.
[31] Voyiadjis GZ, Kattan PI. Mechanics of Composite Materials with MATLAB. Berlin, Heidelberg: Springer; 2005.
[32] Sørensen BF, Goutianos S. Mixed mode cohesive law with interface dilatation. Mech. Mater. 2014;70:76–93.
[33] Goutianos S, Sørensen BF. Fracture resistance enhancement of layered structures by multiple cracks. Eng. Fract. Mech. 2016;151:92–108.
[34] Turon A, Dávila CG, Camanho PP, Costa J. An engineering solution for mesh size effects in the simulation of delamination using cohesive zone models. Eng. Fract. Mech. 2007;74(10):1665–82.

[35] Yang QD, Thouless MD, Ward SM. Numerical simulations of adhesively-bonded beams failing with extensive plastic deformation. J. Mech. Phys. Solids 1999;47:1337–53.

[36] Goutianos S, Sørensen BF. Path dependence of truss-like mixed mode cohesive laws. Eng. Fract. Mech. 2012;91:117–32.

[37] Park, K., Choi, H., Paulino, G.H. Assessment of cohesive traction-separation relationships in abaqus: A comparative study. Mechanics Research Communications 2016;78:71–78. Recent Advances in Multiscale, Multifunctional and Functionally Graded Materials..

[38] Goutianos S, Sørensen BF. The application of J integral to measure cohesive laws under large-scale yielding. Eng. Fract. Mech. 2016;155:145–65.

[39] Belytschko T, Liu WK, Moran B, Elkhodary K. Nonlinear Finite Elements for Continua and Structures. Ltd: John Wiley & Sons; 2000.

[40] Sørensen BF. Microscale testing and modelling for damage tolerant composite materials and structures. IOP Conference Series: Materials Science and Engineering 2020;942:012004.

[41] Sørensen BF, Jacobsen TK. Characterizing delamination of fibre composites by mixed mode cohesive laws. Compos. Sci. Technol. 2009;69(3):445–56.

[42] Holmes JW, Liu L, Sørensen BF, Wahlgren S. Experimental approach for mixed-mode fatigue delamination crack growth with large-scale bridging in polymer composites. J. Compos. Mater. 2014;48(25):3111–28.

[43] Paris P, Erdogan F. A critical analysis of crack propagation laws. Journal of Basic Engineering D 1963;85:528–34.